

1896 **Chapter 9**
1897 **Weak Focusing Synchrotron**

1898 **Abstract** This Chapter introduces to the weak focusing synchrotron, and to the the-
1899 oretical material needed for the simulation exercises. It begins with a brief reminder
1900 of the historical context, and continues with beam optics and acceleration techniques
1901 which the weak focusing synchrotron principle and methods lean on. Regarding the
1902 latter, it relies on basic charged particle optics and acceleration concepts introduced
1903 in the previous Chapters, and further addresses the following aspects:

- 1904 - fixed closed orbit,
- 1905 - periodic structure,
- 1906 - periodic motion stability,
- 1907 - optical functions,
- 1908 - synchrotron motion,
- 1909 - depolarizing resonances.

1910 The simulation of a weak focusing synchrotron lattice only requires two optical
1911 elements: `DIPOLE` or `BEND` to simulate combined function dipoles, and `DRIFT` to
1912 simulate straight sections. A third element `CAVITE`, is required for acceleration. Par-
1913 ticle monitoring requires keywords introduced in the previous Chapters, including
1914 `FAISCEAU`, `FAISTORE`, possibly `PICKUPS`, and some others. Spin motion com-
1915 putation and monitoring resort to `SPNTRK`, `SPNPRT`, `FAISTORE`. Optics matching
1916 and optimization use `FIT[2]`. `INCLUDE` is used, mostly here in order to shorten the
1917 input data files. `SYSTEM` is used to, mostly, resort to `gnuplot` so as to end simu-
1918 lations with some specific graphs obtained by reading data from output files such as
1919 `zgoubi.fai` (resulting from the use of `FAISTORE`), `zgoubi.plt` (resulting from `IL=2`),
1920 or other `zgoubi.*.out` files resulting from a `PRINT` command.

1921 **Notations used in the Text**

$B; \mathbf{B}, B_{x,y,s}$	field value; field vector, its components in the moving frame
$B\rho = p/q; B\rho_0$	particle rigidity; reference rigidity
$C; C_0$	orbit length, $C = 2\pi R + \left[\begin{array}{l} \text{straight} \\ \text{sections} \end{array} \right]$; reference, $C_0 = C(p = p_0)$
E	particle energy
EFB	Effective Field Boundary
$f_{\text{rev}}, f_{\text{rf}}$	revolution and accelerating voltage frequencies
h	RF harmonic number, $h = f_{\text{rf}}/f_{\text{rev}}$
$m; m_0; M$	mass, $m = \gamma m_0$; rest mass; in units of MeV/c ²
$n = \frac{\rho}{B} \frac{dB}{d\rho}$	focusing index
$\mathbf{p}; p; p_0$	momentum vector; its modulus; reference
P_i, P_f	beam polarization, initial, final
q	particle charge
r, R	orbital radius; average radius, $R = C/2\pi$
s	path variable
v	particle velocity
$V(t); \hat{V}$	oscillating voltage; its peak value
x, x', y, y'	horizontal and vertical coordinates in the moving frame

1922

α	momentum compaction
α	trajectory angle
$\beta = v/c; \beta_0; \beta_s$	normalized particle velocity; reference; synchronous
β_u	betatron functions ($u : x, y$)
$\gamma = E/m_0$	Lorentz relativistic factor
δp	momentum offset or Dirac distribution
Δp	momentum offset
ε	wedge angle
ε_u	Courant-Snyder invariant ($u : x, r, y, l, \text{etc.}$)
ε_R	strength of a depolarizing resonance
μ_u	betatron phase advance, $\mu_u = \int_{\text{period}} ds/\beta_u(s)$ ($u : x, y$)
ν_u	wave numbers, radial, vertical, synchrotron ($u : x, y, s$)
ν_{sp}	spin tune
ρ, ρ_0	curvature radius; reference
σ	beam matrix
$\phi; \phi_s$	particle phase at voltage gap; synchronous phase
ϕ_u	betatron phase advance, $\phi_u = \int ds/\beta_u$ ($u : x, y$)
φ	spin angle to the vertical axis

1923 9.1 Introduction

1924 The synchrotron is an outcome of the mid-1940s longitudinal phase focusing syn-
 1925 chronous acceleration concept [1, 2]. In its early version, transverse beam stability
 1926 in the synchrotron during the thousands of turns that the acceleration lasts was based
 1927 on the technique known at the time: weak focusing, as in the cyclotron and in the be-
 1928 tatron. An existing betatron was used to first demonstrate phase-stable synchronous
 1929 acceleration with slow variation of the magnetic field, on a fixed orbit, in 1946 [3],
 1930 - closely following the demonstration of the principle of phase focusing using a
 1931 fixed-field cyclotron [4].

1932 Phase focusing states that stability of the longitudinal motion, longitudinal focus-
 1933 ing, is obtained if particles in a bunch, which have a natural energy spread, arrive
 1934 at the accelerating gap in the vicinity of a proper phase of the oscillating voltage,
 1935 the synchronous phase; if this condition is fulfilled the bunch stays together, in the
 1936 vicinity of the latter, during acceleration. Synchrotrons operate in general in a non-
 1937 isochronous regime: the revolution period changes with energy; as a consequence,
 1938 in order to maintain an accelerated bunch on the synchronous phase, the RF voltage
 1939 frequency, which satisfies $f_{rf} = hf_{rev}$, has to change continuously from injection to
 1940 top energy. The reference orbit in a synchrotron is maintained at constant radius by
 1941 ramping the guiding field in the main dipoles in synchronism with the acceleration,
 1942 as in the betatron [5].

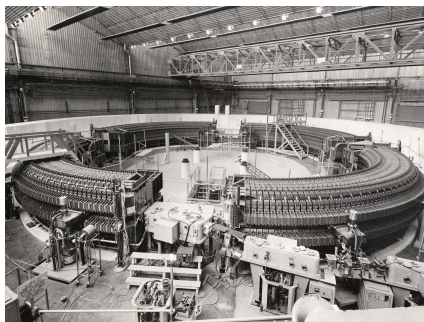


Fig. 9.1 SATURNEI at Saclay [6], a 3 GeV, 4-period, 68.9 m circumference, weak focusing synchrotron, constructed in 1956-58. The injection line can be seen in the foreground, injection is from a 3.6 MeV Van de Graaff (not visible)

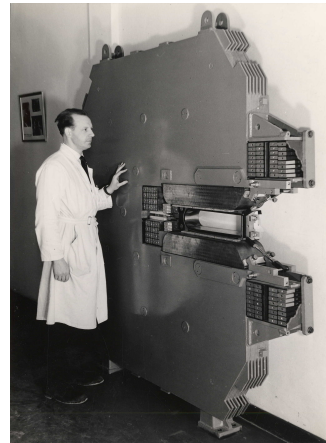


Fig. 9.2 A slice of SATURNEI dipole [6]. The slight gap tapering is hardly visible (increasing outward), it determines the weak index condition $0 < n < 1$

1943 The synchrotron concept allowed the highest energy reach by particle accelerators
 1944 at the time, it led to the construction of a series of proton rings with increasing
 1945 energy [7]: 1 GeV at Birmingham (1953), 3.3 GeV at the Cosmotron (Brookhaven

1946 National Laboratory, 1953-1969), 6.2 GeV at the Bevatron (Berkeley, 1954-1993),
 1947 10 GeV at the Synchro-Phasotron (JINR, Dubna, 1957-2003), and a few additional
 1948 ones in the late 1950s well into the era of the concept which would essentially
 1949 dethrone the weak focusing method and its quite bulky rings of magnets which were
 1950 a practical limit to further increase in energy¹: the strong focusing synchrotron (the
 1951 object of Chapter 10). The general layout of these first weak focusing synchrotrons
 1952 included straight sections (often 4, Fig. 9.1), which allowed insertion of injection
 1953 (Fig. 9.1) and extraction systems, accelerating cavities, orbit correction and beam
 1954 monitoring equipment.

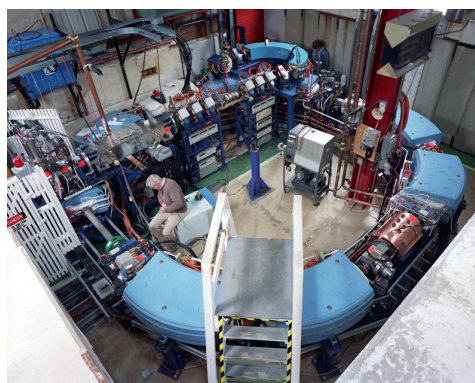


Fig. 9.3 Left: Loma Linda University medical synchrotron [8], during commissioning in 1989 at the Fermilab National Laboratory where it was designed

1955 The next decades following the invention of the synchrotron saw applications in
 1956 many fields of science including fixed-target nuclear physics for particle discovery,
 1957 material science, medicine, industry. Its technological simplicity still makes it an
 1958 appropriate technology today in low energy beam application when relatively low
 1959 current is not a concern, as in the hadrontherapy application (Fig. 9.3) [9, 10]: it
 1960 essentially requires a single type of a simple dipole magnet, an accelerating gap, some
 1961 command-control instrumentation, whereas it procures greater beam manipulation
 1962 flexibilities compared to (synchro-)cyclotrons.

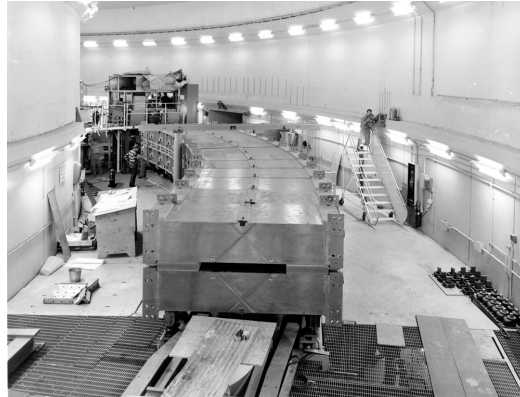
1963 *Polarized beams*

1964 The availability of polarized proton sources allowed the acceleration of polarized
 1965 beams to high energy. The possibility was considered from the early times at Argonne
 1966 ZGS (Zero-Gradient Synchrotron), a 12 GeV weak focusing synchrotron operated
 1967 over 1964-1979 [11] (Fig. 9.4). Up to 70% polarization transmission through the syn-
 1968 chrotron was achieved, for the first time in a synchrotron² and reaching multi-GeV

¹ The story has it that it is possible to ride a bicycle in the vacuum chamber of Dubna's Synchro-Phasotron.

² Polarized beam had been accelerated in cyclotrons, at earlier times.

Fig. 9.4 The ZGS at Argonne during construction. A 12 GeV, 8-dipole, 4-period, 172 m circumference, wedge focusing synchrotron. The two persons inside and outside the ring, in the background, give an idea of the size of the magnets



1969 energy in 1973, up to 17.5 GeV/c with *appreciable polarizations* [12]. Polariza-
 1970 tion preservation techniques included harmonic orbit correction and fast betatron
 1971 tune jump at strongest depolarizing resonances [13] (Fig. 9.16). Experiments were
 1972 performed to assess the possibility of polarization transmission in strong focusing
 1973 synchrotrons, and polarization lifetime in colliders [14]. Acceleration of polarized
 1974 deuteron was achieved in the late 1970s, when sources were made available [15].

1975 9.2 Basic Concepts and Formulae

1976 The synchrotron is based on two key principles. On the one hand, a slowly varying
 1977 magnetic field to maintain a constant orbit during acceleration,

$$B(t) \times \rho = p(t)/q, \quad \rho = \text{constant}, \quad (9.1)$$

1978 with $p(t)$ the particle momentum and ρ the bending radius in the dipoles. On the other
 1979 hand, on synchronous acceleration for longitudinal phase stability. In a regime where
 1980 the velocity change with energy cannot be ignored (non-ultrarelativistic particles),
 1981 the latter requires a modulation of the accelerating voltage frequency so to satisfy

$$f_{rf}(t) = h f_{rev}(t) \quad (9.2)$$

1982 Synchronism between accelerating voltage oscillation and the revolution motion
 1983 keeps the bunch on the synchronous phase at traversal of the accelerating gaps.
 1984 Synchronous acceleration is technologically simpler in the case of electrons, as
 1985 frequency modulation is unnecessary beyond a few MeV; for instance, from $v/c =$
 1986 0.9987 at 10 MeV to $v/c \rightarrow 1$ the relative change in revolution frequency amounts
 1987 to $\delta f_{rev}/f_{rev} = \delta\beta/\beta < 0.0013$.

1988 These are two major evolutions compared to the cyclotron, where, instead, the
 1989 magnetic field is fixed - the reference orbit spirals out, and, by virtue of the isochro-
 1990 nism of the orbits, the oscillating voltage frequency is fixed as well.

1991 A fixed orbit reduces the radial extent of individual guiding magnets, allowing a
 1992 ring structure comprised of a circular string of dipoles. For the sake of comparison:
 1993 a synchrocyclotron instead uses a single, massive dipole; increased energy requires
 1994 increased radial extent of the magnet to allow for the greater bending field integral
 1995 (*i.e.*, $\oint B dl = 2\pi R_{\max} \hat{B} = p_{\max}/q$), thus a volume of iron increasing more than
 1996 quadratically with bunch rigidity.

1997 One or the other of the weak index ($-1 < k < 0$, Sect. 4.2.2) and/or wedge
 1998 focusing (Sect. 15.3.1) are used in weak focusing synchrotrons. Transverse stability
 1999 was based on the latter at Argonne ZGS (Zero-Gradient Synchrotron: the main
 2000 magnet had no field index); ZGS accelerated polarized proton beams, weak focusing
 2001 resulted in weak depolarizing resonances, an advantage in that matter [14].

2002 Due to the necessary ramping of the field, and of the RF frequency to follow,
 2003 in order to maintain a constant orbit, the synchrotron is a pulsed accelerator, the
 2004 acceleration is cycled, from injection to top energy, repeatedly. The repetition rate
 2005 of the acceleration cycle depends on the type of power supply. If the ramping uses a
 2006 constant electromotive force ($E=V+ZI$ is constant), then

$$B(t) \propto (1 - e^{-t/\tau}) = 1 - \left[1 - \left(\frac{t}{\tau}\right) + \left(\frac{t}{\tau}\right)^2 - \dots \right] \approx \frac{t}{\tau} \quad (9.3)$$

2007 essentially linear; $\dot{B} = dB/dt$ does not exceed a few Tesla/second: the repetition rate
 2008 of the acceleration cycle is of the order of a Hertz. If instead the magnet winding
 2009 is part of a resonant circuit then the field oscillates from an injection threshold to a
 2010 maximum value, $B(t) : B_0 \rightarrow B_0 + \hat{B}$, as in the betatron; the repetition rate is up to
 2011 a few tens of Hertz. In both cases anyway B imposes its law and the other quantities
 2012 comprising the acceleration cycle (RF frequency in particular) will follow B(t).

2013 For the sake of comparison: in a synchrocyclotron the field is constant, thus
 2014 acceleration can be cycled as fast as the swing of the voltage frequency allows
 2015 (hundreds of Hz are common practice); assume a conservative 10 kVolts per turn,
 2016 thus of the order of 10,000 turns to 100 MeV, with velocity $0.046 < v/c < 0.43$
 2017 from 1 to 100 MeV, proton. Take $v \approx 0.5c$ to make it simple, an orbit circumference
 2018 below 30 meter, thus the acceleration takes of the order of $10^4 \times C/0.5c \approx$ ms range,
 2019 potentially a repetition rate in kHz range, more than an order of magnitude beyond
 2020 the reach of a rapid-cycling pulsed synchrotron.

2021 9.2.1 Periodic Stability

2022 This section introduces the various components of the transverse focusing and the
 2023 conditions for periodic stability in a weak focusing synchrotron. It builds on material
 2024 introduced in Chap. 4, Classical Cyclotron.

2025 **9.2.1.1 Closed orbit**

2026 The concept is found in the betatron, which accelerates particles on a constant orbit
 2027 (Chap. 7). The closed orbit is fixed, and maintained during acceleration by ensuring
 2028 that the relationship Eq. 9.1 is satisfied. In a perfect ring, the closed orbit is along an
 2029 arc in the bending magnets and straight along the drifts, Fig. 9.5.

2030 Particle motion is defined in a moving frame (O;s,x,y) whose origin coincides
 2031 with the location of an ideal particle following the reference orbit. The moving frame
 2032 s axis is tangent to the reference orbit, its transverse horizontal axis x is normal to
 2033 the s axis, its vertical axis y is normal to the (s,x) plane (Fig. 4.8, Sect. 4.2.2).

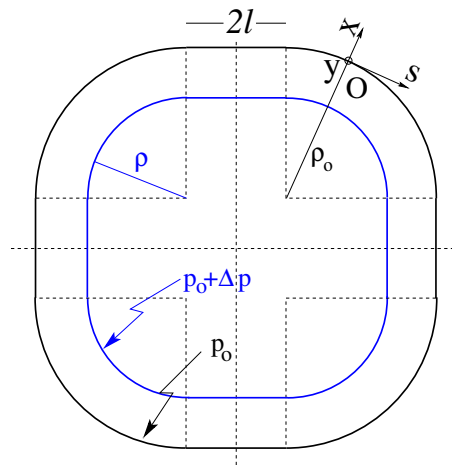


Fig. 9.5 A $2\pi/4$ axially symmetric structure with four drift spaces. Orbit length on reference momentum p_0 is $C = 2\pi\rho_0 + 8l$. (O;s,x,y) is the moving frame, along the reference orbit. The orbit for momentum $p = p_0 + \Delta p$ ($\Delta p < 0$, here) is at constant distance $\Delta x = \frac{\rho_0}{1-n} \frac{\Delta p}{p_0} = \frac{R}{(1+k)(1-n)} \frac{\Delta p}{p_0}$ from the reference orbit

2034 **9.2.1.2 Transverse Focusing**

2035 Radial motion stability around a reference closed orbit in an axially symmetric dipole
 2036 field requires a field index (Sect. 4.2.2),

$$n = -\frac{\rho_0}{B_0} \left. \frac{\partial B_y}{\partial x} \right|_{x=0, y=0} \quad (9.4)$$

2037 a quantity evaluated on the reference arc in the dipoles, satisfying the weak focusing
 2038 condition (Eq. 4.11 with $n = -k$)

$$0 < n < 1 \quad (9.5)$$

2039 This condition can be obtained with a tapered gap (as in SATURNE dipoles, Fig. 9.2)
 2040 causing the magnetic field to decrease slowly with radius, so resulting in both axial

2041 and radial focusing (Figs. 9.6, 9.7). Note the sign convention here, the cyclotron uses
 2042 the opposite sign (Eq. 4.10). This condition holds regardless of the presence of drifts
 2043 or not. Adding drift spaces between the dipoles, the reference orbit is comprised of
 2044 arcs of radius ρ_0 in the magnets, and straight segments along the drift spaces that
 2045 connect these arcs. This requires defining two radii, namely,

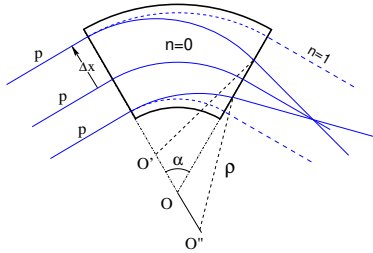


Fig. 9.6 Geometrical focusing: in a sector dipole with focusing index $n = 0$, parallel incoming rays of equal momenta experience the same curvature radius ρ , their trajectories converge as outer trajectories have a longer path in the field, inner ones shorter. An index value $n=1$ cancels that effect: parallel incoming rays exit parallel

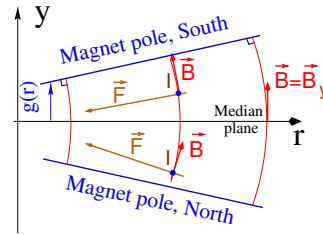


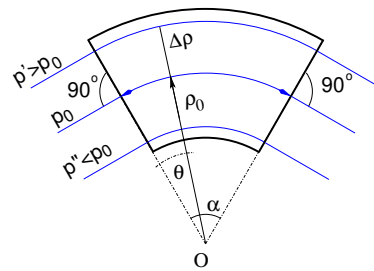
Fig. 9.7 Axial motion stability requires proper shaping of field lines: B_y has to decrease with radius. The Laplace force pulls a positive charge with velocity pointing out of the page, at I, toward the median plane. Increasing the field gradient (n closer to 1, gap opening up faster) increases the focusing

- 2046 (i) the magnet curvature radius ρ_0 ,
 2047 (ii) an average radius $R = C/2\pi = \rho_0 + Nl/\pi$ (with C the length of the reference
 2048 closed orbit and $2l$ the drift length) (Fig. 9.5) which also writes

$$R = \rho_0(1 + k), \quad k = \frac{Nl}{\pi\rho_0} \quad (9.6)$$

2049 Adding drift spaces decreases the average focusing around the ring.

Fig. 9.8 In a sector dipole with radial index $n \neq 0$, closed orbits follow arcs of constant field. A closed orbit at $p_0 + \Delta p$ follows an arc of radius $\rho_0 + \Delta\rho$, $\Delta\rho = \Delta p / (1 + n)qB_0$



2050 *Geometrical focusing*

2051 The limit $n \rightarrow 1$ of the transverse motion stability domain corresponds to a cancel-
 2052 lation of the geometrical focusing (Fig. 9.6): in a constant field dipole (radial field
 2053 index $n=0$) the longer (respectively shorter) path in the magnetic field for parallel
 2054 trajectories entering the magnet at greater (respectively smaller) radius result in
 2055 convergence. This effect is cancelled, *i.e.*, trajectory angle is the same whatever the
 2056 entrance radius, if the curvature center is made independent of the entrance radius:
 2057 $OO' = 0, O''O = 0$. This occurs if trajectories at an outer (inner) radius experience a
 2058 smaller (greater) field such as to satisfy $BL = B\rho\alpha = C^{st}$. Differentiating $B\rho = C^{st}$
 2059 gives $\frac{\Delta B}{B} + \frac{\Delta\rho}{\rho} = 0$, with $\Delta\rho = \Delta x$, so yielding $n = -\frac{\rho_0}{B_0} \frac{\Delta B}{\Delta x} = 1$. The focal distance
 2060 associated with the curvature is (Eq. 4.12 with $R = \rho_0$) $f = \frac{\rho_0^2}{L}$. Optical drawbacks
 2061 of the weak focusing method include the weakness of the focusing and the absence
 2062 of independent radial and axial focusing.

2063 *Wedge Focusing*

2064 Entrance and exit wedge angles may be used to ensure transverse focusing, Fig. 9.9:
 2065 opening the magnetic sector increases the horizontal focusing (and decreases the
 2066 vertical focusing); closing the magnetic sector has the reverse effect (see Sect. 15.3.1).

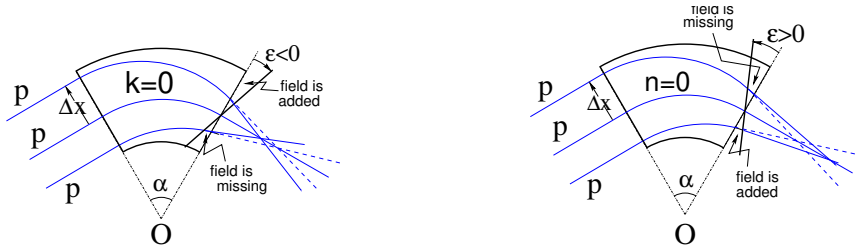


Fig. 9.9 Left: a focusing wedge ($\varepsilon < 0$); opening the sector increases horizontal focusing and decreases vertical focusing. Right: a defocusing wedge ($\varepsilon > 0$), closing the sector, has the reverse effect. This is the origin of the focusing in the ZGS zero-gradient dipoles

2067 In a point transform approximation, at the wedge the trajectory undergoes a local
 2068 deviation proportional to the distance to the optical axis, amounting to

$$\Delta x' = \frac{\tan \varepsilon}{\rho_0} \Delta x, \quad \Delta y' = -\frac{\tan(\varepsilon - \psi)}{\rho_0} \Delta y \quad (9.7)$$

2069 The ψ angle component is a correction for the fringe field extent (Eq. 15.21); the
 2070 effect of the latter, of the first order on the vertical focusing, is of second order
 2071 horizontally.

2072 Profiling the magnet gap in order to adjust the focal distance complicates the
 2073 magnet; a parallel gap, $n = 0$, makes it simpler, for that reason edge focusing may
 2074 be preferred. Wedge vertical focusing in the ZGS ($\varepsilon > 0$) was at the expense of
 2075 horizontal geometrical focusing (Fig. 9.6). This was an advantage though, for the
 2076 acceleration of polarized beams, as radial field components (which are responsible for
 2077 depolarization) were only met at the EFBs of the eight main dipoles, and weak [12].
 2078 Preserving beam polarization at high energy required tight control of the tunes, this
 2079 was achieved by pole face windings added at the ends of the dipoles [16, 17], pulsed
 2080 to control the amplitude detuning, resulting in a control of the tunes at 0.01 level.

2081 9.2.1.3 Betatron motion

2082 The first order differential equations of motion in the moving frame (Fig. 9.5) derive
 2083 from the Lorentz equation

$$\frac{d\mathbf{m}\mathbf{v}}{dt} = q\mathbf{v} \times \mathbf{B} \Rightarrow m \frac{d}{dt} \begin{pmatrix} \frac{ds}{dt} \mathbf{s} \\ \frac{dx}{dt} \mathbf{x} \\ \frac{dy}{dt} \mathbf{y} \end{pmatrix} = q \begin{pmatrix} \left(\frac{dx}{dt} B_y - \frac{dy}{dt} B_x \right) \mathbf{s} \\ -\frac{ds}{dt} B_y \mathbf{x} \\ \frac{ds}{dt} B_x \mathbf{y} \end{pmatrix} \quad (9.8)$$

2084 Motion in a weak index dipole field is solved in Sect. 4.2.2, Classical Cyclotron: in
 2085 the latter substitute ρ to R , $n = -\frac{\rho_0}{B_0} \frac{\partial B_y}{\partial x}$ to $-k$, evaluated on the reference orbit.
 2086 Taylor expansions of the transverse field components in the moving frame (Eq. 4.6)
 2087 lead to

$$\begin{aligned} B_y(\rho)|_{y=0} &= B_0(1 - n \frac{x}{\rho_0}) + \mathcal{O}(x^2) \\ B_x(0+y) &= -n \frac{B_0}{\rho_0} y + \mathcal{O}(y^3) \end{aligned} \quad (9.9)$$

2088 Assume transverse stability: $0 < n < 1$; in the approximation $ds \approx v dt$ (Eq. 4.13)
 2089 Eqs. 9.8, 9.9 lead to the differential equations of motion

$$\frac{d^2x}{ds^2} + \frac{1-n}{\rho_0^2} x = 0, \quad \frac{d^2y}{ds^2} + \frac{n}{\rho_0^2} y = 0 \quad (9.10)$$

2090 It results that, in an S-periodic structure comprised of gradient dipoles, wedges
 2091 and drift spaces, the differential equation of motion takes the general form of Hill's
 2092 equation, a second order differential equation with periodic coefficient, namely (with
 2093 u standing for x or y),

$$\begin{cases} \frac{d^2u}{ds^2} + K_u(s)u = 0 \\ K_u(s+S) = K_u(s) \end{cases} \quad \text{with} \quad \begin{cases} \text{in dipoles : } \begin{cases} K_x = \frac{1-n}{\rho_0^2} \\ K_y = \frac{n}{\rho_0^2} \end{cases} \\ \text{at a wedge at } s = s_0 : K_y = \frac{\pm \tan \varepsilon}{\rho_0} \delta(s - s_0) \\ \text{in drift spaces : } \frac{1}{\rho_0} = 0, K_x = K_y = 0 \end{cases} \quad (9.11)$$

2094 $K_u(s)$ is S-periodic, $S = 2\pi R/N$ ($S = C/4$ for instance in a 4-periodic ring,
2095 Figs. 9.1, 9.5).

2096 The solution of Eqs. 9.11 is not as straightforward as in the cyclotron where K_u is
2097 constant around the ring (Eq. 4.14), which results in a sinusoidal motion (Eq. 4.16)
2098 - the latter is on the other hand a reasonable approximation, see below, *Weak focusing*
2099 *approximation*. G. Floquet has established [18] that the two independent solutions
2100 of Hill's second order differential equation have the form [19]

$$\left\{ \begin{array}{l} u_1(s) = \sqrt{\beta_u(s)} e^{i \int_0^s \frac{ds}{\beta_u(s)}} \\ du_1(s)/ds = \frac{i - \alpha_u(s)}{\beta_u(s)} u_1(s) \end{array} \right. \quad \text{and} \quad \left\{ \begin{array}{l} u_2(s) = u_1^*(s) \\ du_2(s)/ds = du_1^*(s)/ds \end{array} \right. \quad (9.12)$$

2101 wherein $\beta_u(s)$ and $\alpha_u(s) = -\beta'_u(s)/2$ are S-periodic functions, from what it results
2102 that

$$u_{\frac{1}{2}}(s+S) = u_{\frac{1}{2}}(s) e^{\pm i \mu_u} \quad (9.13)$$

2103 wherein

$$\mu_u = \int_{s_0}^s \frac{ds}{\beta_u(s)} \quad (9.14)$$

2104 is the betatron phase advance at s , from the origin s_0 . A real solution of Hill's
2105 equation is the linear combination $A u_1(s) + A^* u_2^*(s)$. With $A = \frac{1}{2} \sqrt{\varepsilon_u/\pi} e^{i\phi}$
2106 following conventional notations, ϕ the phase of the motion at the origin $s = s_0$, the
2107 general solution of Eq. 9.11 writes

$$\left\{ \begin{array}{l} u(s) = \sqrt{\beta_u(s) \varepsilon_u/\pi} \cos\left(\int_{s_0}^s \frac{ds}{\beta_u} + \phi\right) \\ u'(s) = -\sqrt{\frac{\varepsilon_u/\pi}{\beta_u(s)}} \sin\left(\int_{s_0}^s \frac{ds}{\beta_u} + \phi\right) + \alpha_u(s) \cos\left(\int_{s_0}^s \frac{ds}{\beta_u} + \phi\right) \end{array} \right. \quad (9.15)$$

2108 An invariant of the motion, known as the Courant-Snyder invariant, is

$$\frac{1}{\beta_u(s)} \left[u^2 + (\alpha_u(s)u + \beta_u(s)u')^2 \right] = \frac{\varepsilon_u}{\pi} \quad (9.16)$$

2109 At a given azimuth s of the periodic structure the observed turn-by-turn motion
2110 lies on that ellipse (Fig. 9.10). The form and inclination of the ellipse depend on
2111 the observation azimuth s via the respective local values of $\alpha_u(s)$ and $\beta_u(s)$, but
2112 its surface ε_u is invariant. Motion along the ellipse is clockwise, as can be figured
2113 from Eq. 9.15 considering an observation azimuth s where the ellipse is upright,
2114 $\alpha_u(s) = 0$. The phase advance over a turn (from one position to the next on the
2115 ellipse, Fig. 9.10) in an N-periodic ring yields the wave number

$$\nu_u = N\mu_u = \int_{s_0}^{s_0+NS} \frac{ds}{\beta_u(s)} = N \int_{\text{period}} \frac{ds}{\beta_u(s)} \quad (9.17)$$

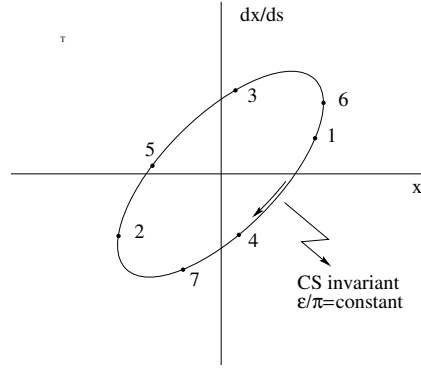


Fig. 9.10 Courant-Snyder invariant and turn-by-turn harmonic motion along the invariant, observed at some azimuth s . The form and tilt-angle of the ellipse depend on the observation azimuth s but its surface ε_u is invariant

2116 *Weak focusing approximation*

2117 In a cylindrically symmetric structure a sinusoidal motion is the exact solution of the
 2118 first order differential equations of motion (Eqs. 4.15, 4.16, Classical Cyclotron Chap-
 2119 ter), the coefficients $K_x = (1 - n)/R_0^2$ and $K_y = n/R_0^2$ are constant (s -independent).
 2120 Adding drift spaces results in Hill's differential equation with periodic coefficient
 2121 $K(s+S) = K(s)$ (Eq. 9.11), and in a pseudo harmonic solution (Eq. 9.15). Due to the
 2122 weak focusing the beam envelope is only weakly modulated (see below), thus so is
 2123 $\beta_u(s)$. In a practical manner, the modulation of $\beta_u(s)$ does not exceed a few percent,
 2124 this justifies introducing the average value $\bar{\beta}_u$ to approximate the phase advance by

$$\int_0^s \frac{ds}{\beta_u(s)} \approx \frac{s}{\bar{\beta}_u} = \nu_u \frac{s}{R} \quad (9.18)$$

2125 The right equality is obtained by applying this approximation to the phase advance
 2126 per period, namely (Eq. 9.14) $\mu_u = \int_{s_0}^{s_0+S} \frac{ds}{\beta_u(s)} \approx S/\bar{\beta}_u$, and introducing the wave
 2127 number of the N -period optical structure $\nu_u = \frac{N\mu_u}{2\pi} = \frac{\text{phase advance over a turn}}{2\pi}$ so that

$$\bar{\beta}_u = \frac{R}{\nu_u} \quad (9.19)$$

2128 the wavelength of the betatron oscillation around the ring. With $k \ll 1$ and using
 2129 Eq. 9.23,

$$\bar{\beta}_x = \frac{\rho_0(1+k/2)}{\sqrt{1-n}}, \quad \bar{\beta}_y = \frac{\rho_0(1+k/2)}{\sqrt{n}} \quad (9.20)$$

2130 Substituting $\nu_u \frac{s}{R}$ to $\int \frac{ds}{\beta_u(s)}$ in Eq. 9.15 yields the approximate solution

$$\begin{cases} u(s) \approx \sqrt{\beta_u(s)\varepsilon_u/\pi} \cos\left(\nu_u \frac{s}{R} + \phi\right) \\ u'(s) \approx -\sqrt{\frac{\varepsilon_u/\pi}{\beta_u(s)}} \sin\left(\nu_u \frac{s}{R} + \phi\right) + \alpha_u(s) \cos\left(\nu_u \frac{s}{R} + \phi\right) \end{cases} \quad (9.21)$$

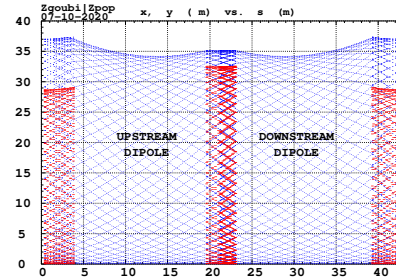
2131 *Beam envelopes*

2132 The beam envelope $\hat{u}(s)$ (with u standing for x or y) is determined by the particle of
 2133 maximum invariant ε_u/π , it is given at all s by

$$\hat{u}_{\text{env}}(s) = \pm \sqrt{\beta_u(s) \frac{\varepsilon_u}{\pi}} \quad (9.22)$$

As $\beta_u(s)$ is S -periodic, so is the envelope, $\hat{u}(s+S) = \hat{u}(s)$. In a cell with symmetries,

Fig. 9.11 Multi-turn particle excursion along the ZGS 2-dipole 43 m cell. The motion extrema (Eq. 9.22) tangent the envelopes, respectively horizontal (red), and vertical (blue). Envelops have the symmetry of the cell



2134 beam envelopes feature the same symmetries, as in Fig. 9.11 for instance: a symmetry
 2135 with respect to the center of the cell; envelop extrema are at azimuth s of $\beta_u(s)$
 2136 extrema, *i.e.* where $d\hat{u}(s)/ds \propto \beta'_u(s) = 0$ or $\alpha_u = 0$ as $\beta'_u = -2\alpha_u$.
 2137

2138 *Working point*

2139 The “working point” of the synchrotron is the wave number couple (ν_x, ν_y) at which
 2140 the accelerator is operated, it fully characterizes the focusing. In a structure with
 2141 cylindrical symmetry (such as the Classical Cyclotron) $\nu_x = \sqrt{1-n}$ and $\nu_y = \sqrt{n}$
 2142 (Eq. 4.17) so that $\nu_x^2 + \nu_y^2 = 1$: when the radial field index n is changed the working
 2143 point stays on a circle of radius 1 in the stability diagram (or “tune diagram”,
 2144 Fig. 9.12). If drift spaces are added, from Eqs. 9.19, 9.20, with $1 + \frac{k}{2} \approx \sqrt{R/\rho_0}$
 2145 (Eq. 9.6), it comes

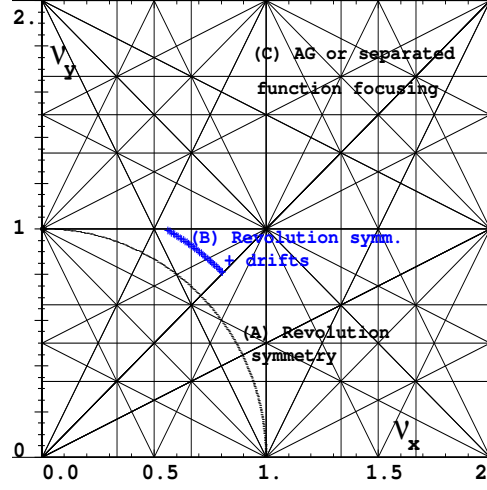
$$\nu_x \approx \sqrt{(1-n) \frac{R}{\rho_0}}, \quad \nu_y \approx \sqrt{n \frac{R}{\rho_0}}, \quad \nu_x^2 + \nu_y^2 \approx \frac{R}{\rho_0} \quad (9.23)$$

thus the working point is located on the circle of radius $\sqrt{R/\rho_0} > 1$ (Fig. 9.12), tunes
 can not exceed the limits

$$0 < \nu_{x,y} \lesssim \sqrt{R/\rho_0}$$

2146 Horizontal and vertical focusing are not independent (Eq. 9.11): if ν_x increases then
 2147 ν_y decreases and reciprocally. This is a lack of flexibility which the advent of strong

Fig. 9.12 Location of the working point in the tune diagram. (A) field with revolution symmetry: (ν_x, ν_y) is on a circle of radius 1; (B) sector field with index $0 < n < 1$ and drift spaces: (ν_x, ν_y) is on a circle of radius $(\sqrt{R/\rho_0})$; (C) strong focusing, AG index $|n| \gg 1$ or separated function, ν_x and ν_y are large, set independently



2148 focusing will overcome by providing two knobs allowing separate adjustment of the
2149 tunes.

2150 *Off-momentum orbits; periodic dispersion*

2151 In the linear approximation in $\Delta p/p_0$, a momentum offset $\Delta p = p - p_0$ changes
2152 mv to $mv(1 + \Delta p/p_0)$ in Eq. 9.8; this changes the horizontal equation of motion
2153 (Eq. 9.10) to

$$\frac{d^2x}{ds^2} + K_x x = \frac{1}{\rho_0} \frac{\Delta p}{p_0}, \quad \text{or} \quad \frac{d^2x}{ds^2} + K_x \left(x - \frac{1}{\rho_0 K_x} \frac{\Delta p}{p_0} \right) = 0 \quad (9.24)$$

2154 A change of variable $x - \frac{1}{K_x \rho_0} \frac{\Delta p}{p_0} \rightarrow x$ (with $1/\rho_0 K_x = \rho_0/(1-n)$) restores the
2155 unperturbed equation of motion; thus orbits of different momenta $p = p_0 + \Delta p$ are
2156 distant

$$\Delta x = \frac{\rho_0}{1-n} \frac{\Delta p}{p_0} \quad (9.25)$$

2157 from the reference orbit (Fig. 9.8). Introduce the geometrical radius $R = (1+k)\rho_0$
2158 (Eq. 9.6) to account for the added drifts; this yields the dispersion function

$$D_x = \frac{\Delta x}{\Delta p/p_0} \equiv \frac{\Delta R}{\Delta p/p_0} = \frac{R}{(1-n)(1+k)} = \frac{\rho_0}{1-n}, \quad \text{constant, positive} \quad (9.26)$$

2159 D_x is the chromatic dispersion of the orbits, an s-independent quantity: in a structure
2160 with axial symmetry, comprising drift sections (Fig. 9.5) or not (classical and AVF

2161 cyclotrons for instance), the ratio $\frac{\Delta x}{\rho_0 \Delta p / p_0}$ is independent of the azimuth s , the
 2162 distance of a chromatic orbit to the reference orbit is constant around the ring.

2163 Given that $n < 1$,

2164 - higher momentum orbits, $p > p_0$, have a greater radius,

2165 - lower momentum orbits, $p < p_0$, have a smaller radius.

2166 The horizontal motion of an off-momentum particle is a superposition of the
 2167 betatron motion (solution of Hill's Eq. 9.21 with $\delta p / p = 0$) and of a particular
 2168 solution of the inhomogeneous equation ($\delta p / p \neq 0$), namely

$$x(s) = \sqrt{\beta_u(s)\epsilon_u/\pi} \cos\left(v_u \frac{s}{R} + \phi\right) + \frac{\rho_0}{1-n} \frac{\Delta p}{p_0} \quad (9.27)$$

2169 whereas the vertical motion is unchanged.

2170 Chromatic orbit length

2171 In an axially symmetric structure the difference in closed orbit length $\Delta C = 2\pi\Delta R$
 2172 resulting from the difference in momentum arises in the dipoles, as all orbits are
 2173 parallel in the drifts (Fig. 9.5). Hence, from Eq. 9.26, the relative closed orbit
 2174 lengthening factor, or momentum compaction

$$\alpha = \frac{\Delta C}{C} \Big/ \frac{\Delta p}{p_0} \equiv \frac{\Delta R}{R} \Big/ \frac{\Delta p}{p_0} = \frac{1}{(1-n)(1+k)} \approx \frac{1}{v_x^2} \quad (9.28)$$

2175 with $k = Nl/\pi\rho_0$ (Eq. 9.6). Note that the relationship $\alpha \approx 1/v_x^2$ between momentum
 2176 compaction and horizontal wave number established for a revolution symmetry
 2177 structure (Eq. 4.21) still holds when adding drifts.

2178 9.2.2 Acceleration

In a synchrotron, the field B is varied during acceleration (a function performed by the magnet power supply) concurrently with the variation of the bunch momentum p (a function performed by the accelerating cavity) in such a way that the beam is maintained on the design orbit. Given the energies involved, the magnet supply imposes its law $B(t)$ (Fig. 9.13) and the cavity follows, the best it can. The accelerating voltage $\hat{V}(t) = \sin \omega_{rf}t$ is maintained in synchronism with the revolution motion, its angular frequency satisfying

$$\omega_{rf} = h\omega_{rev} = h \frac{c}{R} \frac{B(t)}{\sqrt{\left(\frac{m_0 c}{q\rho}\right)^2 + B^2(t)}}$$

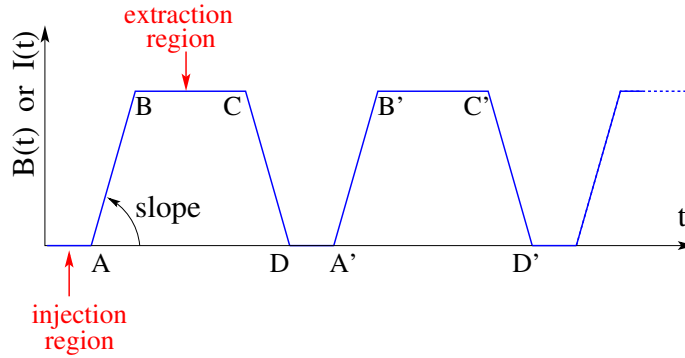


Fig. 9.13 Cycling $B(t)$ in a pulsed synchrotron. Ignoring saturation, $B(t)$ is proportional to the magnet power supply current $I(t)$. Beam injection occurs at low field, in the region of A, extraction occurs at top energy, on the high field plateau. (AB): field ramp up (acceleration); (BC): flat top; (CD): field ramp down; (DA'): thermal relaxation. (AA'): repetition period; $(1/AA')$: repetition rate; *slope*: ramp velocity $\dot{B} = dB/dt$ (Tesla/s).

Typically, for a $C = 2\pi R \approx 70$ m circumference ring (SATURNE I weak focusing synchrotron, Fig. 9.1; cf. Exercise 9.1, parameters in Tab. 9.1), from $\beta = v/c \approx 0.09$ at injection (3.6 MeV protons) to $\beta \approx 1$ at top energy (3 GeV), the revolution period $T_{\text{rev}} = C/\beta c$ and frequency $\omega_{\text{rev}}/2\pi = 1/T_{\text{rev}}$ span

$$\begin{cases} T_{\text{rev}} : 2.6 \mu\text{s} \rightarrow 23 \mu\text{s} \\ f_{\text{rev}} : 390 \text{ kHz} \rightarrow 4.3 \text{ MHz} \end{cases}$$

2179 *Energy gain*

2180 The variation of the particle energy over a turn amounts to the work of the force
2181 $F = dp/dt = q\rho dB/dt$ on the charge at the cavity, namely

$$\Delta W = F \times 2\pi R = 2\pi R q \rho \dot{B} \quad (9.29)$$

In a slow-cycling synchrotron \dot{B} is usually constant over most of the acceleration cycle (Eq. 9.3), thus so is ΔW . At SATURNE I for instance

$$\frac{\Delta W}{q} = 2\pi R \rho \dot{B} = 68.9 \times 8.42 \times 1.8 = 1044 \text{ volts}$$

The field ramp lasts

$$\Delta t = (B_{\text{max}} - B_{\text{min}})/\dot{B} \approx B_{\text{max}}/\dot{B} = 0.8 \text{ s}$$

The number of turns to the top energy ($W_{\text{max}} \approx 3$ GeV) is

$$N = \frac{W_{\max}}{\Delta W} = \frac{3 \cdot 10^9 \text{ eV}}{1044 \text{ eV/turn}} \approx 3 \cdot 10^6 \text{ turns}$$

The dependence of particle mass on field writes

$$m(t) = \gamma(t)m_0 = \frac{q\rho}{c} \sqrt{\left(\frac{m_0 c}{q\rho}\right)^2 + B(t)^2}$$

2182 *Adiabatic damping of the betatron oscillations*

Particle momentum increases at the accelerating gap, this results in a decrease of the amplitude of betatron oscillations (conversely, an increase if the cavity is decelerating). The mechanism is sketched in Fig. 9.14 (with u standing indifferently for the x or y coordinate): the slope, respectively before and after (index 2) the cavity is

$$\frac{du}{ds} = \frac{m \frac{du}{dt}}{m \frac{ds}{dt}} = \frac{p_u}{p_s}, \quad \frac{du}{ds} \Big|_2 = \frac{m \frac{du}{dt} \Big|_2}{m \frac{ds}{dt} \Big|_2} = \frac{p_{u,2}}{p_{s,2}}$$

As the kick in momentum is longitudinal, $dp_u/dt = 0$ thus $p_{u,2} = p_u$, the increase

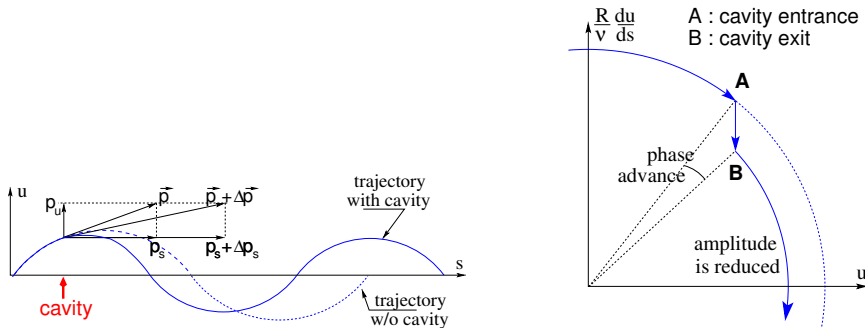


Fig. 9.14 Adiabatic damping of betatron oscillations, here from trajectory incidence $u' = p_u/p_s$ at cavity entrance, to $u'_2 = p_u/(p_s + \Delta p_s)$ at cavity exit. In the transverse phase space: decrease of the particle phase space invariant resulting from $\Delta \left(\frac{du}{ds} \right)$

in momentum is purely longitudinal, $p_{s,2} = p_s + \Delta p_s$. Thus

$$\frac{du}{ds} \Big|_2 = \frac{p_u}{p_s + \Delta p_s} \approx \frac{p_u}{p_s} \left(1 - \frac{\Delta p_s}{p_s} \right)$$

and as a consequence the slope du/ds varies across the cavity,

$$\Delta \left(\frac{du}{ds} \right) = \frac{du}{ds} \Big|_2 - \frac{du}{ds} = - \frac{du}{ds} \frac{\Delta p_s}{p_s}$$

2183 The variation of the slope is proportional to the slope, with opposite sign if $\Delta p/p > 0$
 2184 (acceleration) thus a decrease of the slope. This variation has two consequences on
 2185 the betatron oscillation (Fig. 9.14):
 2186 - a change of the betatron phase,
 2187 - a modification of the betatron amplitude.

2188 *Coordinate transport*

2189 at the cavity writes $\begin{cases} u_2 = u \\ u'_2 \approx \frac{p_u}{p_s} (1 - \frac{dp}{p}) = u' (1 - \frac{dp}{p}) \end{cases}$. In matrix form, $\begin{pmatrix} u_2 \\ u'_2 \end{pmatrix} =$
 2190 $[C] \begin{pmatrix} u \\ u' \end{pmatrix}$ with

$$[C] = \begin{bmatrix} 1 & 0 \\ 0 & 1 - \frac{dp}{p} \end{bmatrix} \quad (9.30)$$

2191 and $\det[C] = 1 - \frac{dp}{p} \neq 1$: the system is non-conservative, the surface of the beam
 2192 ellipse in phase space is not conserved. Assume one cavity in the ring and note
 2193 $[T] \times [C]$ the one-turn coordinate transport matrix with origin at entrance of the
 2194 cavity. Its determinant is $\det[T] \times \det[C] = \det[C] = 1 - \frac{dp}{p}$; the variation of
 2195 the transverse ellipse surface satisfies $\varepsilon_u = (1 - \frac{dp}{p_0})\varepsilon_0$ or, with $d\varepsilon_u = \varepsilon_u - \varepsilon_0$,
 2196 $\frac{d\varepsilon_u}{\varepsilon_u} = -\frac{dp}{p_0}$, the solution of which is

$$p \varepsilon_u = \text{constant, or } \beta\gamma\varepsilon_u = \text{constant} \quad (9.31)$$

2197 Over N turns the coordinate transport matrix is $[T_N] = ([T][C])^N$, thus the ellipse
 2198 surface changes by a factor $\det[C]^N = (1 - \frac{dp}{p})^N \approx 1 - N\frac{dp}{p}$.

2199 *Phase stability*

2200 “Synchrotron motion” designates the mechanism of phase stability, or longitudinal
 2201 focusing (Fig. 9.15), that stabilizes the longitudinal motion of a particle in the vicinity
 2202 of a synchronous phase, ϕ_s , in virtue of

2203 (i) the presence of an accelerating cavity with its frequency indexed on the
 2204 revolution time,

2205 (ii) with the bunch centroid positioned either on the rising slope of the oscillating
 2206 voltage (low energy regime), or on the falling slope (high energy regime).

The synchronous (or “ideal”) particle follows the equilibrium trajectory around
 the ring (the reference closed orbit, about which all other particles will undergo a
 betatron oscillation), its velocity satisfies $v(t) = \frac{qB\rho(t)}{m}$; at each turn it reaches the
 accelerating gap when the oscillating voltage is at the synchronous phase ϕ_s , and
 undergoes an energy gain

$$\Delta W = q\hat{V} \sin \phi_s$$

The condition $|\sin \phi_s| < 1$ imposes a lower limit to the cavity voltage for acceleration to happen, namely, after Eq. 9.29,

$$\hat{V} > 2\pi R \rho \dot{B}$$

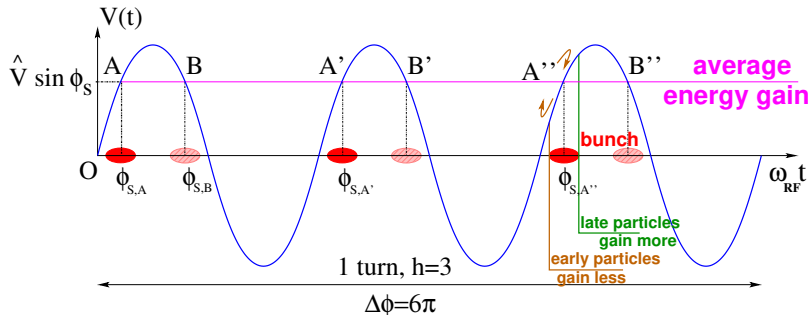


Fig. 9.15 A sketch of the mechanism of phase stability, $h = 3$ in this example. Below transition phase stability occurs for a synchronous phase taken at either one of A, A', A'' arrival times at the gap: a particle with a little greater energy compared to the synchronous particle goes around the ring more rapidly than the latter: if both are launched together, the former arrives earlier at the voltage gap (at $\phi < \phi_{s,A}$) and thus experiences weaker acceleration; a particle with a little lower energy compared to the synchronous particle, is slower, it arrives at the gap later, $\phi > \phi_{s,A}$, and thus experiences greater voltage; in both cases the particle is pulled towards the synchronous phase, this results in an overall stable oscillatory motion around the synchronous phase. Beyond transition the stable phase is at either one of B, B', B'' locations: a particle which is less energetic than the synchronous particle arrives earlier, $\phi < \phi_{s,B}$, so experiencing a greater voltage, and inversely, resulting in overall stable synchrotron motion.

2207 Referring to Fig. 9.15, the synchronous phase can be placed on the left (A A' A''...
 2208 series in the Figure, or on the right (B B' B''... series) of the oscillating voltage crest.
 2209 One and only one of these two possibilities, and which one depending upon the optical
 2210 lattice and on particle energy, ensures that particles in a bunch remain grouped in
 2211 the vicinity of the synchronous particle. The transition is between two time-of-flight
 2212 regimes: a particle which gains momentum compared to the synchronous particle
 2213 has a greater velocity, while
 2214 - in the high bunch energy regime the increase in path length around the ring
 2215 is faster than the increase in velocity (velocity essentially does not even change
 2216 in ultrarelativistic regime), a revolution around the ring takes more time (this is the
 2217 classical cyclotron and synchrocyclotron regime, and as well the high energy electron
 2218 synchrotron regime); consider such a particle, arriving at the accelerating gap late
 2219 ($\phi(t) > \phi_s$), in order for it to be pulled toward bunch center (*i.e.*, take less time
 2220 around the ring) it has to undergo deceleration; this is the B series, above transition;
 2221 - in the low bunch energy regime velocity increase is faster than path length
 2222 increase, thus a revolution around the ring is faster; consider such a particle, arriving
 2223 at the accelerating gap early ($\phi(t) < \phi_s$), in order for it to be pulled toward bunch

center (*i.e.*, take more time around the ring) it has to be slowed down, it has to undergo deceleration; this is the A series, below transition.

Transition energy

The transition between the two time-of-flight regimes occurs at $\frac{dT_{\text{rev}}}{T_{\text{rev}}} = 0$. With $T = 2\pi/\omega = C/v$, this can be written $\frac{d\omega_{\text{rev}}}{\omega_{\text{rev}}} = -\frac{dT_{\text{rev}}}{T_{\text{rev}}} = \frac{dv}{v} - \frac{dC}{C}$. With $\frac{dv}{v} = \frac{1}{\gamma^2} \frac{dp}{p}$ and momentum compaction $\alpha = \frac{dC}{C} / \frac{dp}{p}$, (Eq. 9.28), this can be written

$$\frac{d\omega_{\text{rev}}}{\omega_{\text{rev}}} = -\frac{dT_{\text{rev}}}{T_{\text{rev}}} = \left(\frac{1}{\gamma^2} - \alpha \right) \frac{dp}{p} = \eta \frac{dp}{p} \quad (9.32)$$

which introduces the phase-slip factor

$$\eta = \overbrace{\frac{1}{\gamma^2}}^{\text{kinematics}} - \underbrace{\alpha}_{\text{lattice}} = \frac{1}{\gamma^2} - \frac{1}{\gamma_{\text{tr}}^2} \quad (9.33)$$

The transition γ_{tr} appears to be a property of the lattice.

In a weak focusing lattice $\gamma_{\text{tr}} = 1/\sqrt{\alpha} \approx \nu_x$ (Eqs. 4.21, 9.28), thus the phase stability regime is

$$\begin{aligned} &\text{below transition, } i.e. \phi_s < \pi/2, \quad \text{if } \gamma < \nu_x \\ &\text{above transition, } i.e. \phi_s > \pi/2, \quad \text{if } \gamma > \nu_x \end{aligned} \quad (9.34)$$

In a weak focusing synchrotron the horizontal tune $\nu_x = \sqrt{(1-n)R/\rho_0}$ (Eq. 9.23) may be ≥ 1 , and subsequently $\gamma_{\text{tr}} > 1$ is a possibility. There is no transition-gamma if $\nu_x < 1$. At SATURNE I for instance, with $\nu_x \approx 0.7$ (Tab. 9.1) thus $\gamma_{\text{tr}} < 1$, ramping in energy did not require transition-gamma crossing³.

9.2.3 Depolarizing Resonances

The field index is essentially zero in the ZGS, transverse focusing is ensured by wedge angles at the ends of the height dipoles, the only location where non-zero radial field components are found. The latter are weak, as a consequence so are depolarizing resonances: “As we can see from the table, the transition probability

³ Transition-gamma crossing, or “gamma jump”, is a common beam manipulation during acceleration in strong focusing synchrotrons, it requires an RF phase jump, the technique is addressed in Chapter 10.

2243 [from spin state $\psi_{1/2}$ to spin state $\psi_{-1/2}$] is reasonably small up to $\gamma = 7.1$ [12], i.e.
 2244 $G\gamma = 12.73$, $p = 6.6$ GeV/c; the table referred to stipulates a transition probability
 2245 $P_{\frac{1}{2},-\frac{1}{2}} < 0.042$, whereas resonances beyond that energy range feature $P_{\frac{1}{2},-\frac{1}{2}} > 0.36$.
 2246 Beam depolarization up to 6 GeV/c, under the effect of these resonances, is illustrated
 2247 in Fig. 9.16.

2248 In a synchrotron using gradient dipoles, particles experience radial fields $B_x(y) =$
 2249 $-n \frac{B_0}{\rho_0} y$ as they undergo vertical betatron oscillations [12, 20, 21]. As n is small these
 2250 radial field components are weak, and so is their effect on spin motion.

Assuming a defect-free ring, the vertical betatron motion excites “intrinsic” spin resonances, located at

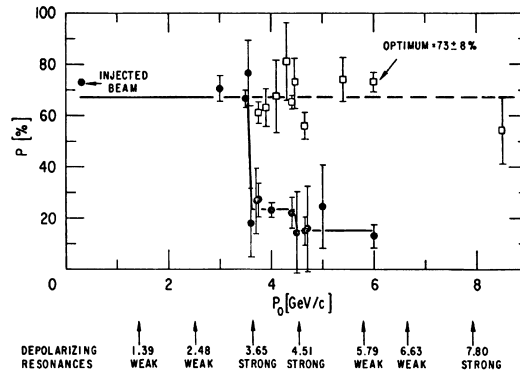
$$G\gamma_R = k P \pm \nu_y$$

with k an integer and P the period of the ring. In the ZGS for instance, $\nu_y \approx 0.8$ (Tab. 9.2), the ring is $P=4$ -periodic, thus $G\gamma_R = 4k \pm 0.8$. Strongest resonances are located at

$$G\gamma_R = mk P \pm \nu_y$$

2251 with m the number of cells per superperiod [22, Sec. 3.II]. In the ZGS, $m=2$ thus
 2252 strongest resonances occur at $G\gamma_R = 2 \times 4k \pm 0.8 = 7.2$ ($p = 3.65$ GeV/c), 8.8 (4.51 GeV/c), 15.2 (7.9 GeV/c), ... (Fig. 9.16).

Fig. 9.16 Polarization loss at the ZGS [23] through the strong intrinsic resonances $G\gamma_R = 7.2$ ($p = 3.65$ GeV/c) and 8.8 (4.51 GeV/c) (black circles). A tune jump method preserves polarization (empty circles)



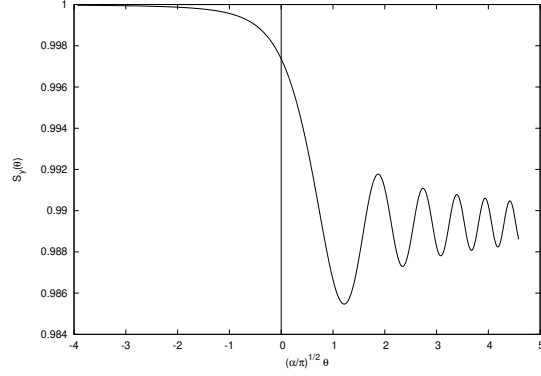
2253 In the presence of vertical orbit defects, non-zero periodic transverse fields are experienced along the closed orbit, they excite “imperfection” depolarizing resonances, located at

$$G\gamma_R = k$$

with k an integer. In the case of systematic defects the periodicity of the orbit is that of the lattice, P , imperfection resonances are located at $G\gamma_R = kP$. Strongest imperfection resonances are located at [22, Sec. 3.II]

$$G\gamma_R = mk P$$

Fig. 9.17 Vertical component of spin motion $S_y(\theta)$ through a weak depolarizing resonance (Eq. 9.41). The vertical bar is at the location of the resonance, which coincides with the origin of the orbital angle



2254 Crossing an isolated depolarizing resonance (Figs. 9.16, 9.17) causes a loss of
2255 polarization given by the Froissart-Stora formula [24] [21, Sect. 2.3.6], ,

$$\frac{P_f}{P_i} = 2e^{-\frac{\pi}{2} \frac{|\epsilon_R|^2}{\alpha}} - 1 \quad (9.35)$$

2256 from a value P_i upstream to an asymptotic value P_f downstream of the resonance.
2257 ϵ_R is the strength of the resonance [21, Sect. 2.3.5], and

$$\alpha = G \frac{dy}{d\theta} = \frac{1}{2\pi} \frac{\Delta E}{M} \quad (9.36)$$

2258 is the crossing speed for an energy gain ΔE per turn.

2259 *Spin precession axis. Resonance width*

2260 Consider the spin vector $\mathbf{S}(\theta) = (S_\eta, S_\xi, S_y)$ of a particle in the laboratory frame,
2261 with θ the orbital angle around the accelerator. Introduce the projection $s(\theta)$ of \mathbf{S} in
2262 the median plane

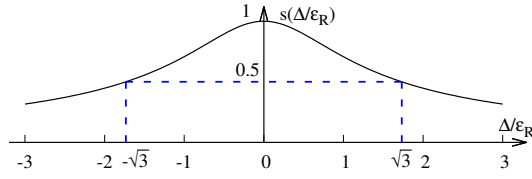
$$s(\theta) = S_\eta(\theta) + jS_\xi(\theta) \quad (\text{and } S_y^2 = 1 - s^2) \quad (9.37)$$

2263

2264 In the case of a stationary solution of the spin motion, viz. stationary spin preces-
2265 sion axis around the ring, s satisfies [21] (Fig. 9.18)

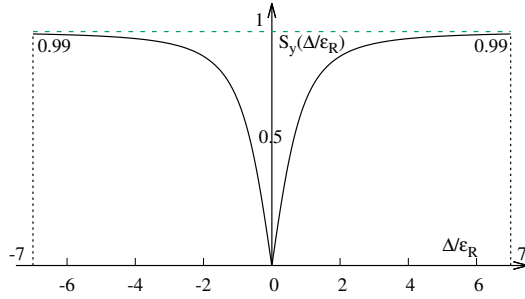
$$s^2 = \frac{1}{1 + \frac{\Delta^2}{|\epsilon_R|^2}} \quad (9.38)$$

Fig. 9.18 Modulus of the horizontal spin component. $s = 1/2$ at distance $\Delta = \pm\sqrt{3}\epsilon_R$ from $G\gamma_R$



2266 with $\Delta = G\gamma - G\gamma_R$ the distance to the resonance; thus the resonance width appears to be a measure of its strength. The quantity of interest is the angle, ϕ , of the spin

Fig. 9.19 Dependence of polarization on the distance to the resonance. For instance $S_y = 0.99$, 1% depolarization, corresponds to $\Delta = \pm 7|\epsilon_R|$. On the resonance, $\Delta = 0$, the precession axis lies in the median plane, $S_y = 0$



2267 precession direction to the vertical axis, given by (Fig. 9.19)

$$\cos \phi(\Delta) \equiv S_y(\Delta) = \sqrt{1 - s^2} = \frac{\Delta/|\epsilon_R|}{\sqrt{1 + \Delta^2/|\epsilon_R|^2}} \quad (9.39)$$

2269 On the resonance, $\Delta = 0$, the spin precession axis lies in the bend plane: $\phi = \pm\pi/2$.
 2270 $S_y = 0.99$ (1% depolarization) corresponds to a distance to the resonance $\Delta = 7|\epsilon_R|$,
 2271 spin precession axis at an angle $\phi = \arccos(0.99) = 8^\circ$ from the vertical.

2272 Conversely, given S_y ,

$$\frac{\Delta^2}{|\epsilon_R|^2} = \frac{S_y^2}{1 - S_y^2} \quad (9.40)$$

The precession axis is common to all spins, S_y is a measure of the polarization along the vertical axis,

$$S_y = \frac{N^+ - N^-}{N^+ + N^-}$$

2273 wherein N^+ and N^- denote the number of particles in spin states $\frac{1}{2}$ and $-\frac{1}{2}$ respectively.
 2274

2275 *Spin motion through weak resonances*

Depolarizing resonances are weak up to several GeV in a weak focusing synchrotron, as the radial and/or longitudinal fields are weak. Thus assume $S_{y,f} \approx S_{y,i}$, with $S_{y,f}$ and $S_{y,i}$ the asymptotic vertical spin component values respectively upstream and downstream of the resonance; with the origin of the orbital angle taken at the resonance (Fig. 9.17), and introducing the Fresnel integrals [21]

$$C(x) = \int_0^x \cos\left(\frac{\pi}{2}t^2\right) dt, \quad S(x) = \int_0^x \sin\left(\frac{\pi}{2}t^2\right) dt$$

2276 the polarization satisfies

$$\begin{aligned} \text{if } \theta < 0 : \left(\frac{S_y(\theta)}{S_{y,i}}\right)^2 &= 1 - \frac{\pi|\epsilon_R|^2}{\alpha} \left\{ \left[\frac{1}{2} - C\left(-\theta\sqrt{\frac{\alpha}{\pi}}\right) \right]^2 + \left[\frac{1}{2} - S\left(-\theta\sqrt{\frac{\alpha}{\pi}}\right) \right]^2 \right\} \\ \text{if } \theta > 0 : \left(\frac{S_y(\theta)}{S_{y,i}}\right)^2 &= 1 - \frac{\pi|\epsilon_R|^2}{\alpha} \left\{ \left[\frac{1}{2} + C\left(\theta\sqrt{\frac{\alpha}{\pi}}\right) \right]^2 + \left[\frac{1}{2} + S\left(\theta\sqrt{\frac{\alpha}{\pi}}\right) \right]^2 \right\} \end{aligned} \quad (9.41)$$

2277 In the asymptotic limit,

$$\frac{S_y(\theta)}{S_{y,i}} \xrightarrow{\theta \rightarrow \infty} 1 - \frac{\pi}{\alpha} |\epsilon_R|^2 \quad (9.42)$$

2278 which identifies with the development of Froissart-Stora formula, Eq. 9.35, to the
2279 first order in $|\epsilon_R|^2/\alpha$. This approximation holds in the limit that higher order terms
2280 can be neglected: $|\epsilon_R|^2/\alpha \ll 1$.

2281 **9.3 Exercises**2282 **9.1 Construct SATURNE I (weak index) synchrotron. Spin Resonances**

2283 Solution: page 311.

2284 In this exercise, the weak focusing 3 GeV synchrotron SATURNE I is modeled.
2285 Spin resonances in a weak dipole gradient lattice are observed.

2286 (a) Construct a model of SATURNE I 90° cell dipole in the hard-edge model,
2287 using DIPOLE. Use the parameters given in Tab. 9.1, and Fig. 9.20 as a guidance. In
2288 order to allow beam monitoring, split the dipole in two 45° deg halves. It is judicious
2289 to take RM=841.93 cm in DIPOLE, as this is the reference radius for the definition
2290 of the radial index. Take an integration step size in centimeter range - small enough
2291 to ensure numerical convergence, as large as doable for fast multiturn raytracing.

2292 Validate the model by producing the 6×6 transport matrix of the cell dipole
2293 (MATRIX[IFOC=0] can be used for that, with OBJET[KOBJ=5] to define a proper
2294 set of paraxial initial coordinates) and checking against theory (Sect. 15.2, Eq. 15.6).

Table 9.1 Parameters of SATURNEI weak focusing synchrotron [25]. ρ_0 denotes the reference bending radius in the dipole; the reference orbit, field index, wave numbers, etc., are taken along that radius

Orbit length, C	cm	6890
Average radius, $R = C/2\pi$	cm	1096.58
Drift length, $2l$	cm	400
Magnetic radius, ρ_0	cm	841.93
$R/\rho_0 = 1 + k$		1.30246
Field index n , nominal		0.6
Wave numbers ν_x, ν_y , nominal		0.72, 0.89
Stability limit		$0.5 < n < 0.757$
Injection energy (proton)	MeV	3.6
Field at injection	kG	0.326
Top energy	GeV	2.94
Field at top energy, B_{\max}	kG	14.9
\dot{B}	kG/s	18
Synchronous energy gain	keV/turn	1.160
RF harmonic		2

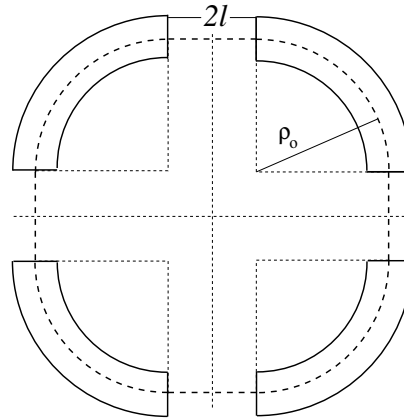


Fig. 9.20 A schematic layout of SATURNEI, a $2\pi/4$ axial symmetry structure, comprised of 4 radial field index 90° dipoles and 4 drift spaces. The cell in the simulation exercises is taken as a $\pi/2$ quadrant: half-drift / 90° -dipole / half-drift

- 2295 (b) Construct a model of SATURNEI cell, with origin at the center of the drift.
 2296 Find the closed orbit, that particular trajectory which has all its coordinates zero in
 2297 the drifts: use DIPOLE[KPOS] to cancel the closed orbit coordinates at DIPOLE
 2298 ends. While there, check the expected value of the dispersion (Eq. 9.26) and of
 2299 the momentum compaction (Eq. 9.28), from the raytracing of a chromatic closed
 2300 orbit - *i.e.*, the orbit of an off-momentum particle. Plot these two orbits (on- and
 2301 off-momentum), over a complete turn around the ring, on a common graph.
 2302 Compute the cell periodic optical functions and tunes, using either MA-
 2303 TRIX[IFOC=11] or TWISS; check their values against theory. Check consistency
 2304 with previous dispersion function and momentum compaction outcomes.
 2305 Move the origin of the lattice at a different azimuth s along the cell: verify that,
 2306 while the transport matrix depends on the origin, its trace does not.

2307 Produce a graph of the optical functions (betatron functions and dispersion) along
2308 the cell. Check the expected average values of the betatron functions (Eq. 9.20).

2309 Produce a scan of the tunes over the field index range $0.5 \leq n \leq 0.757$. RE-
2310 BELOTE can be used to repeatedly change n over that range. Superimpose the
2311 theoretical curves $\nu_x(n)$, $\nu_y(n)$.

(c) Justify considering the betatron oscillation as sinusoidal, namely,

$$y(\theta) = A \cos(\nu_y \theta + \phi)$$

2312 wherein $\theta = s/R$, $R = \oint ds/2\pi$.

2313 (d) Launch a few particles evenly distributed on a common paraxial horizontal
2314 Courant-Snyder invariant, vertical motion taken null (OBJET[KOBJ=8] can be used),
2315 for a single pass through the cell. Store particle data along the cell in zgoubi.plt,
2316 using DIPOLE[IL=2] and DRIFT[split,N=20,IL=2]. Use these to generate a graph
2317 of the beam envelopes.

2318 Using Eq. 9.22 compare with the results obtained in (b). Find the minimum
2319 and maximum values of the betatron functions, and their azimuth $s(\min[\beta_x])$,
2320 $s(\max[\beta_x])$. Check the latter against theory.

2321 Repeat for the vertical motion, taking $\varepsilon_x = 0$, ε_y paraxial.

2322 Repeat, using, instead of several particles on a common invariant, a single particle
2323 traced over a few tens of turns.

2324 (e) Produce an acceleration cycle from 3.6 MeV to 3 GeV, for a few particles
2325 launched on a common $10^{-4} \pi m$ initial invariant in each plane. Ignore synchrotron
2326 motion (CAVITE[IOP=3] can be used in that case). Take a peak voltage $\hat{V} = 200$ kV
2327 (unrealistic though, as it would result in a nonphysical \dot{B} (Eq. 9.29)) and synchronous
2328 phase $\phi_s = 150$ deg (justify $\phi_s > \pi/2$).

2329 Check the betatron damping over the acceleration range: compare with theory
2330 (Eq. 9.31).

2331 How close to symplectic the numerical integration is (it is by definition *not*
2332 symplectic, being a truncated Taylor series method [26, Eq. 1.2.4]), depends on the
2333 integration step size, and on the size of the flying mesh in the DIPOLE method [26,
2334 Fig. 20]; check a possible departure of the betatron damping from theory as a function
2335 of these parameters.

2336 Produce a graph of the horizontal and vertical wave number values over the
2337 acceleration cycle.

2338 (f) Some spin motion, now. Adding SPNTRK at the beginning of the sequence
2339 used in (e) will ensure spin tracking.

2340 Based on the input data file worked out for question (d), simulate the acceleration
2341 of a single particle, through the intrinsic resonance $G\gamma_R = 4 - \nu_Z$, from a distance
2342 of a few times the resonance strength upstream (this requires determining BORO
2343 value under OBJET) to a distance of a few times the resonance strength downstream
2344 of the resonance, at an acceleration rate of 10 kV/turn.

2345 OBJET[KOBJ=8] can be used to allow to easily define an initial invariant value.

2346 On a common graph, plot $S_y(\text{turn})$ for a few different values of the vertical
2347 betatron invariant (the horizontal invariant value does not matter - explain that

2348 statement, it can be taken zero). Derive the resonance strength from these tracking,
2349 check against theory.

2350 Repeat, for different crossing speeds instead.

2351 Push the tracking past beyond $G\gamma = 2 \times 4 + \nu_y$: verify that the sole systematic
2352 resonances $G\gamma = \text{integer} \times P \pm \nu_y$ are excited - with $P = 4$ the periodicity of the
2353 ring.

2354 Break the 4-periodicity of the lattice by perturbing the index in one of the 4
2355 dipoles (say, by 10%). Push the tracking beyond $G\gamma = 2 \times 4 + \nu_y$: verify that all
2356 resonances $G\gamma = \text{integer} \pm \nu_y$ are excited.

2357 (g) Considering a weak resonance crossing, single particle (*i.e.*, a case where
2358 $P_f/P_i \approx 1$, taken from (f); crossing speed may be increased, or particle invariant
2359 decreased), show that it satisfies Eq. 9.41. Match its tracking data to Eq. 9.41 so to
2360 get the vertical betatron tune ν_y , the location of the resonance $G\gamma_R$, and its strength.

2361 (h) Spin motion at fixed energy is considered in this question. Track a few particles
2362 with distances from the resonance $\Delta = G\gamma - G\gamma_R = G\gamma - (4 - \nu_y)$ evenly spanning
2363 the interval $\Delta \in [0, 7 \times \epsilon_R]$.

2364 Produce on a common graph the spin motion $S_y(\text{turn})$ for these particles, as
2365 observed at some azimuth along the ring.

Produce a graph of $\langle S_y \rangle|_{\text{turn}}(\Delta)$ (as in Fig. 9.19). Produce the vertical betatron
tune ν_y , the location of the resonance $G\gamma_R$, and its strength, obtained from a match
of $\langle S_y \rangle|_{\text{turn}}(\Delta)$ to (Eq. 9.39)

$$\langle S_y \rangle (\Delta) = \frac{\Delta}{\sqrt{|\epsilon_R|^2 + \Delta^2}}$$

2366 (i) Track a 200-particle 6-D bunch, with Gaussian transverse densities of $\epsilon_{Y,Z}$ a
2367 few μm , and Gaussian $\delta p/p$ with $\sigma_{\delta p/p} = 10^{-4}$. Produce a graph of the average
2368 value of S_Z over a 200 particle set, as a function of $G\gamma$, across the $G\gamma_R = 4 - \nu_Z$
2369 resonance. Indicate on that graph the location of the resonant $G\gamma_R$ values.

2370 Perform this resonance crossing for five different values of the particle invariant:
2371 $\epsilon_Z/\pi = 2, 10, 20, 40, 200 \mu\text{m}$. Compute P_f/P_i in each case, check the dependence
2372 on ϵ_Z against theory.

2373 Compute the resonance strength, ϵ_Z , from these tracking.

2374 Re-do this crossing simulation for a different crossing speed (take for instance
2375 $\hat{V} = 10 \text{ kV}$) and a couple of vertical invariant values, compute P_f/P_i so obtained.
2376 Check the crossing speed dependence of P_f/P_i against theory.

2377 9.2 Construct the ZGS (zero-gradient) synchrotron. Spin Resonances

2378 Solution: page 336.

2379 In this exercise, the ZGS 12 GeV synchrotron is modeled. Spin resonances in a
2380 zero-gradient, wedge focusing synchrotron are studied.

2381 A photo taken in the ZGS tunnel is given in Fig. 9.4; a schematic layout of the ring
2382 is shown in Fig. 9.21, and a sketch of the double dipole cell in Fig. 9.22. Table 9.2
2383 details the parameters of the synchrotron resorted to in these simulations.

2384 (a) Construct a model of ZGS 45° cell dipole in the hard-edge model, using
 2385 DIPOLE. Use the parameters given in Tab. 9.2, and Figs. 9.21, 9.22 as a guidance.
 2386 In order to allow beam monitoring, split the dipole in two 22.5° deg halves. Take the
 2387 closed orbit radius as the reference RM=2076 cm in DIPOLE: it will be assumed
 2388 that the orbit is the same at all energies⁴. Take an integration step size in centimeter
 2389 range - small enough to ensure numerical convergence, as large as doable for fast
 2390 multiturn raytracing.

2391 Validate the model by producing the 6 × 6 transport matrices of both dipole
 2392 (MATRIX[IFOC=0] can be used for that, with OBJET[KOBJ=5] to define a proper
 2393 set of paraxial initial coordinates) and checking against theory (Sect. 15.2, Eq. 15.6).

2394 Add fringe fields in DIPOLE[λ, C₀ - C₅], the rest if the exercise will use that
 2395 model. Take fringe field extent and coefficient values

$$\lambda = 60 \text{ cm } C_0 = 0.1455, C_1 = 2.2670, C_2 = -0.6395, C_3 = 1.1558, C_4 = C_5 = 0 \quad (9.43)$$

2396 (C₀ - C₅ determine the shape of the field fall-off, they have been computed from a
 2397 typical measured field profile $B(s)$).

2398 (b) Construct a model of ZGS cell accounting for dipole fringe fields, with origin
 2399 at the center of the long drift. In doing so, use DIPOLE[KPOS] to cancel the closed
 2400 orbit coordinates at DIPOLE ends.

2401 Compute the periodic optical functions at cell ends, and cell tunes, using MA-
 2402 TRIX[IFOC=1 1]; check their values against theory.

2403 Move the origin at the location (azimuth s along the cell) of the betatron functions
 2404 extrema: verify that, while the transport matrix depends on the origin, its trace does
 2405 not. Verify that the local betatron function extrema, and the dispersion function, have
 2406 the expected values.

2407 Produce a graph of the optical functions (betatron functions and dispersion) along
 2408 the cell.

2409 (c) Additional verifications regarding the model.

2410 Produce a graph of the field $B(s)$

2411 - along the on-momentum closed orbit, and along off-momentum chromatic closed
 2412 orbits, across a cell;

2413 - along orbits at large horizontal excursion;

2414 - along orbits at large vertical excursion.

2415 For all these cases, verify qualitatively, from the graphs, that $B(s)$ appears as
 2416 expected.

(d) Justify considering the betatron oscillation as sinusoidal, namely,

$$y(\theta) = A \cos(\nu_y \theta + \phi)$$

2417 wherein $\theta = s/R$, $R = \oint ds/2\pi$.

2418 (e) Produce an acceleration cycle from 50 MeV to 17 GeV about, for a few particles
 2419 launched on a common $10^{-5} \pi \text{ m}$ vertical initial invariant, with small horizontal
 2420 invariant. Ignore synchrotron motion (CAVITE[IOPT=3] can be used in that case).

⁴ Note that in reality the reference orbit in ZGS moved outward during acceleration [27].

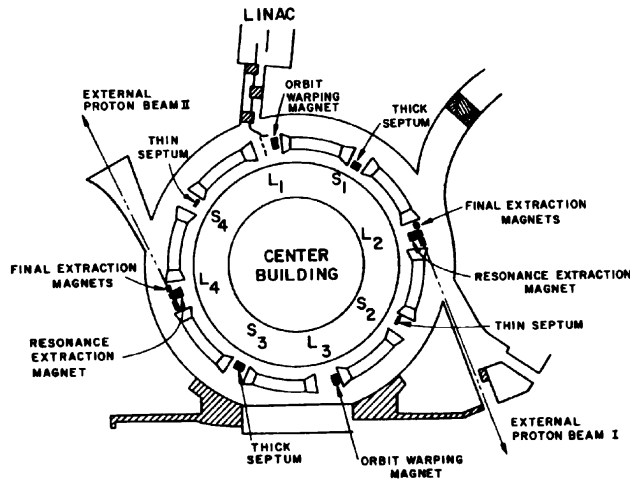


Fig. 9.21 A schematic layout of the ZGS [23], a $\pi/2$ -periodic structure, comprised of 8 zero-index dipoles, 4 long and 4 short straight sections

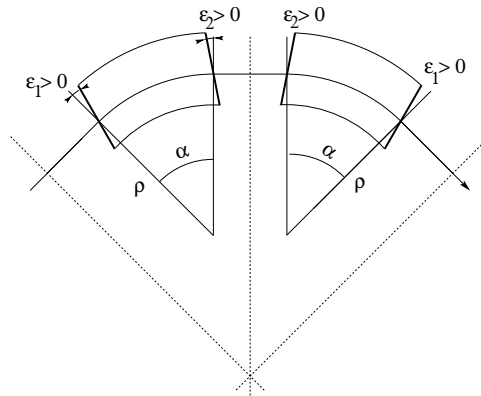


Fig. 9.22 A sketch of ZGS cell layout. In defining the entrance and exit faces (EFBs) of the magnet, beam goes from left to right. Wedge angles at the long straight sections (ϵ_1) and at the short straight sections (ϵ_2) are different

2421 Take a peak voltage $\hat{V} = 200\text{ kV}$ (this is unrealistic but yields 10 times faster
 2422 computing than the actual $\hat{V} = 20\text{ kV}$, Tab. 9.2) and synchronous phase $\phi_s = 150\text{ deg}$
 2423 (justify $\phi_s > \pi/2$). Add spin, using SPNTRK, in view of the next question, (f).

2424 Check the accuracy of the betatron damping over the acceleration range, compared
 2425 to theory. How close to symplectic the numerical integration is (it is by definition
 2426 *not* symplectic), depends on the integration step size, and on the size of the flying
 2427 mesh in the DIPOLE method [26, Fig. 20]; check a possible departure of the betatron
 2428 damping from theory as a function of these parameters.

2429 Produce a graph of the evolution of the horizontal and vertical wave numbers
 2430 during the acceleration cycle.

Table 9.2 Parameters of the ZGS weak focusing synchrotron after Refs. [27, 28][23, pp.288-294,p.716] (2nd column, when they are known) and in the present simplified model and numerical simulations (3rd column). Note that the actual orbit moves during ZGS acceleration cycle, tunes change as well - this is not taken into account in the present modeling, for simplicity

		From Refs. [27, 28]	Simplified model
Injection energy	MeV		50
Top energy	GeV		12.5
$G\gamma$ span		1.888387 - 25.67781	
Length of central orbit	m	171.8	170.90457
Length of straight sections, total	m	41.45	40.44
<i>Lattice</i>			
Wave numbers $\nu_x; \nu_y$		0.82; 0.79	0.849; 0.771
Max. $\beta_x; \beta_y$	m		32.5; 37.1
<i>Magnet</i>			
Length	m	16.3	16.30486 (magnetic)
Magnetic radius	m	21.716	20.76
Field min.; max.	kG	0.482; 21.5	0.4986; 21.54
Field index			0
Yoke angular extent	deg	43.02590	45
Wedge angle	deg	≈ 10	13 and 8
<i>RF</i>			
Rev. frequency	MHz	0.55 - 1.75	0.551 - 1.751
RF harmonic $h=\omega_{rf}/\omega_{rev}$			8
Peak voltage	kV	20	200
B-dot, nominal/max.	T/s	2.15/2.6	
Energy gain, nominal/max.	keV/turn	8.3/10	100
Synchronous phase, nominal	deg		150
<i>Beam</i>			
$\varepsilon_x; \varepsilon_y$ (at injection)	$\pi\mu\text{m}$		25; 150
Momentum spread, rms			3×10^{-4}
Polarization at injection	%	>75	100
Radial width of beam (90%), at inj.	inch	2.5	$\sqrt{\beta_x \varepsilon_x / \pi} = 1.1$

2431 (f) Using the raytracing material developed in (e): produce a graph of the vertical
 2432 spin component of the particles, and the average value over that 200 particle set, as
 2433 a function of $G\gamma$. Indicate on that graph the location of the resonant $G\gamma_R$ values.

- 2434 (g) Based on the simulation file used in (f), simulate the acceleration of a single
 2435 particle, through one particular intrinsic resonance, from a few thousand turns
 2436 upstream to a few thousand turns downstream.
- 2437 Perform this resonance crossing for different values of the particle invariant.
 2438 Determine the dependence of final/initial vertical spin component value, on the
 2439 invariant value; check against theory.
- 2440 Re-do this crossing simulation for a different crossing speed. Check the crossing
 2441 speed dependence of final/initial vertical spin component so obtained, against theory.
- 2442 (h) Introduce a vertical orbit defect in the ZGS ring.
 2443 Find the closed orbit.
- 2444 Accelerate a particle launched on that closed orbit, from 50 MeV to 17 GeV about,
 2445 produce a graph of the vertical spin component.
- 2446 Select one particular resonance, reproduce the two methods of (g) to check the
 2447 location of the resonance at $G\gamma_R = \text{integer}$, and to find its strength.

2448 References

- 2449 1. Veksler, V.: A new method of acceleration of relativistic particles. J. of Phys. USSR 9 153-158
 2450 (1945)
- 2451 2. McMillan, E. M.: The Synchrotron. Phys. Rev. 68 143-144 (1945)
- 2452 3. Goward, F. K., and Barnes, D. E.: Experimental 8 MeV synchrotron for electron acceleration.
 2453 Nature 158, 413 (1946)
- 2454 4. Richardson, J.R., et al.: Frequency Modulated Cyclotron. Phys. Rev. 69: 669 (1946)
- 2455 5. Kerst, D. W.: The Acceleration of Electrons by Magnetic Induction.. Phys. Rev., 60, 47-53
 2456 (1941)
- 2457 6. SATURNEI photos: FAR_SA_N_00248, FAR_SA_N_02826; credit CEA Saclay. Archives
 2458 historiques CEA. Copyright CEA/Service de documentation
- 2459 7. Sessler, A., Wilson, E.: Engines of Discovery. A Century of Particle Accelerators. World
 2460 Scientific, 2007
- 2461 8. Fig. 9.3: Credit Reider Hahn, Fermilab
- 2462 9. Endo, K., et al.: Compact proton and carbon ion synchrotrons for radiation therapy. MOPRI087,
 2463 Proceedings of EPAC 2002, Paris, France; pp. 2733-2735.
 2464 <https://accelconf.web.cern.ch/e02/PAPERS/MOPRI087.pdf>
- 2465 10. Vostrikov, V.A., et al.: Novel approach to design of the compact proton synchrotron magnetic
 2466 lattice. tupsa17, 26th Russian Particle Accelerator Conference RUPAC2018, Protvino, Russia
 2467 (2018).
 2468 <https://accelconf.web.cern.ch/rupac2018/papers/tupsa17.pdf>
- 2469 11. Cohen, D., : Feasibility of Accelerating Polarized Protons with the Argonne ZGS. Review of
 2470 Scientific Instruments 33, 161 (1962).// <https://doi.org/10.1063/1.1746524>
- 2471 12. Ratner, L.G. and Khoe, T.K.: Acceleration of Polarized Protons in the Zero Gradient Syn-
 2472 chrotron. Procs. PAC 1973 Conference, Washington (1973).
 2473 http://accelconf.web.cern.ch/p73/PDF/PAC1973_0217.PDF
- 2474 13. Bywatwr, J., Khoe, T., et al.: A pulsed quadrupole system for preventing depolarization. IEEE
 2475 Transactions on Nuclear Science (Volume: 20, Issue: 3, June 1973)
- 2476 14. Cho, Y., et als.: Effects of depolarizing resonances on a circulating beam of polarized protons
 2477 during or storage in a synchrotron. IEEE Trans. Nuclear Science, Vol.NS-24, No.3, June 1977
- 2478 15. Parker, E.F.: High Energy Polarized Deuterons at the Argonne National Laboratory Zero
 2479 Gradient Synchrotron. IEEE Transactions on Nuclear Science, Vol. NS-26, No. 3, June 1979,
 2480 pp 3200-3202